Electronic Supplementary Material (ESI) for Journal of Materials Chemistry A.

Supplementary Information

Defect-Activated Surface Reconstruction: Mechanism for Triggering Oxygen Evolution Reaction Activity of NiFe Phosphide

Tong Chen[a, b], Bing Li[a, b], Kai Song[a, b], Chenxu Wang[a, b], Jiawei Ding[a, b], Enzuo Liu[a, b], Biao Chen[a, b], Fang He[a, b]*

[a] School of Materials Science and Engineering, Tianjin University, Tianjin, 300350, P.R. China.

[b] Tianjin Key Laboratory of Composite and Functional Materials, Tianjin University, Tianjin, 300350, P.R. China.

*Corresponding Author. E-mail: fanghe@tju.edu.cn.

1. Supplementary Methods

1.1 Chemical and materials

Carbon cloth (CC) was purchased from Guangdong New Energy Technology Co., Ltd. $Ni(NO_3)_2 \cdot 6H_2O$, $Fe(NO_3)_3 \cdot 9H_2O$, $Zn(NO_3)_2 \cdot 6H_2O$, Urea ($(NH_4)_2CO$), and KOH were purchased from Shanghai Aladdin Biochemical Technology Co., Ltd. Ammonium fluoride (NH_4F) was purchased from Tianjin Jiangtian Chemical Technology Co., Ltd. Sodium hypophosphite (NaH_2PO_2) was purchased from K-Mart (Tianjin) Chemical Technology Co., Ltd. All chemical reagents used in this research were of analytical grade.

1.2 Synthesis of self-supporting catalysts

Synthesis of Zn-NiFe LDH precursor. The precursors were grown on the CC by a hydrothermal method. Firstly, CC was pretreated with HNO_3 solution (65%) for 12 h to remove surface impurity, and then rinsed with ultrapure water and absolute ethanol. Second, 9 mmol $Ni(NO_3)_2 \cdot 6H_2O$, 3 mmol $Fe(NO_3)_2 \cdot 9H_2O$, 3 mmol $Zn(NO_3)_2 \cdot 6H_2O$, 14 mmol NH_4F, and 36 mmol Urea were dissolved in 80 ml deionized water. The aqueous solution and pre-cleaned CC were then transferred to a Teflon-lined autoclave, which was heated to 120 ℃ and held there for 6 hours.

Synthesis of Zn-NiFeP/CC. The CC coated with the precursor of Zn-NiFeP was removed after natural cooling to 25 ℃, cleaned with deionized water, and properly dried at 60 ℃. The Zn-NiFe LDH/CC precursor was then created by phosphatizing the precursor at 300 ℃ for 3 hours in an Ar environment. In this phosphatization process, the NaH_2PO_2 as the phosphorus source was put into the porcelain boat on the upstream side and the CC with the precursor was placed on the downstream side.

Synthesis of d-NiFeP/CC. To create cationic vacancy defects, the above Zn-NiFeP sample was then immersed in 0.5 M H_2SO_4 solution and acid-etched for 24 hours. Finally, the black color NiFeP nanosheet arrays with cationic vacancy defect on CC substrate was rinsed with distilled water and dried in an oven.

Synthesis of NiFeP/CC. For comparison, the pure NiFeP/CC sample was also prepared under a similar condition to Zn-NiFeP/CC sample except for 3 mmol $Zn(NO_3)_2 \cdot 6H_2O$, which was used during the hydrothermal process.

1.3 Characterization

X-ray diffraction (XRD) measurements were carried out by using Bruker D8 Advance X-ray diffractometer with a Cu Kα line of 0.1541 nm. The characterization of the material morphology using a thermal field emission scanning electron microscope (SEM, JSM-7800F) in high vacuum mode, transmission electron microscopy (TEM, JEM-2100F) measurements were tested at 200 kV and 120 μA, combined with energy dispersive X-ray spectroscopy (EDX) to examine the material morphology and elemental distribution. The phase composition and chemical bonding properties in the samples are characterized by Raman spectroscopy (RAMAN, Renishaw inVia). The spot size of the laser for Raman spectroscopy is 0.9 μm. The wavelength of the laser for Raman spectroscopy is 532nm. The power of the laser for Raman spectroscopy is 90 mW. X-ray photoelectron spectroscopy (XPS) measurements were achieved on Axis Supra with an Al Kα source. Elemental content was analyzed by inductively coupled plasma optical emission spectrometry (ICP-OES, Agilent 5110).

1.4 Electrochemical measurements

Electrochemical characterization of catalyst is performed in a three-electrode configuration immersed in 1.0 M potassium hydroxide (KOH, pH=13.8). The electrocatalytic properties of samples were studied in a three-electrode system, in which the prepared catalytic electrode (0.5 cm × 0.5 cm) was used as the working electrode, a graphite rod was used as the counter electrode, and Hg/HgO electrode was utilized as the reference electrode. To prepare Pt/C and RuO_2 electrodes as control samples, Pt/C and RuO_2 powders were loaded on CC with a loading of 0.4 mg cm^{-2}. Before recording the electroactivity of catalysts, 20 cycles of cyclic voltammetry (CV) scans with a scan rate of 50 mV s^{-1}. LSV measurements with a scan rate of 5 mV s^{-1} are carried out to record the current density-potential data of the catalyst. The potentials were all calibrated to reversible hydrogen electrode (RHE) using the following equation: E(RHE) = E(Hg/HgO) + 0.0591 × pH + 0.098. The Tafel slope is calculated by the equation: $\eta = a + b \times \log(j)$, where η is the overpotential, j is the current density, and b is the Tafel slope. EIS measurements were also performed from 10000 Hz to 0.1 Hz. In addition, the C_{dl} of the catalyst is estimated from CV measurements over a non-Faraday potential interval at different scan rates. ECSA is calculated according to the equation $ECSA = C_{dl} / C_s$, where C_s = 0.04 mF cm^{-2}. 3000 CV cycles were performed to evaluate the durability of the material at a scan rate of

100 mV S^{-1}, and the corresponding LSV curves were recorded before and after the cycles, with the interval chosen between 1.22 and 1.52 V (*vs.* RHE) for OER and between 0 and -0.25 V (*vs.* RHE) for HER. For OWS, the voltage range for the CV cycles is 1.4 V to 1.8 V.

1.5 Density functional theory calculation

All calculations are performed using the first-principles calculations method based on density functional theory (DFT) as implemented in the Vienna ab initio Simulation Package (VASP) [1, 2]. The projector-augmented wave pseudopotential is used to describe ionic cores [3]. The electronic exchange and correlation is described by using Perdew-Burke-Ernzerhof (PBE) functional within the generalized gradient approximation (GGA) [4]. The convergence criterion was set to be 1.0×10^{-5} eV/atom, and the atomic structures are fully relaxed until the force on each atom is less than 0.02 eV/Å for geometry optimizations [5]. The valence electrons of all the atoms are described using a plane wave basis set with 400 eV energy cutoff. Spin polarization is considered in all calculations. The vacuum of 15 Å was employed to eliminate the influence of periodic boundary conditions. The (1 1 1) surface of Ni_2P and the (0 1 2) surface of NiOOH were chosen as the base models, and the surfaces were doped with Fe atoms. For Ni_2P, the k-points sampling of the Brillouin zone is (4 × 4 × 1) grid with the gamma (Γ) point for geometry relaxation. And the k-point sampling for NiOOH is a (1 × 3 × 1) grid.

OER Process: The OER process is a four-step reaction with the following reaction equation for each step:

(1) $H_2O + * \rightarrow *OH + *H + e^-$

(2) $*OH \rightarrow *O + *H + e^-$

(3) $*O + H_2O \rightarrow *OOH + *H + e^-$

(4) $*OOH \rightarrow O_2 + *H + e^-$

Here, the thermochemistry of electrochemical reactions is modeled based on density flooding calculations. The Gibbs free energy is obtained as a descriptor to evaluate the catalytic activity using corrections added to the calculated DFT energy through entropy (TS) and zero-point energy (ZPE) contributions：

$\Delta G = \Delta E + \Delta ZPE - T\Delta S$

ΔZPE is the change in ZPE calculated from the vibration frequency and ΔS is the change in entropy. The free energy of adsorption of each oxygen-containing substance can be described

by the following equation:

$\Delta G(*OH) = G(*OH) + 0.5G(H_2) - G(slab) - G(H_2O)$

$\Delta G(*O) = G(*O) + G(H_2) - G(slab) - G(H_2O)$

$\Delta G(*OOH) = G*OOH + 1.5G(H_2) - G(slab) - 2G(H_2O)$

where G((*OH), G((*O) and G((*OOH) are the total energies of *OH, *O and *OOH substances adsorbed on the plate. G(slab), $G(H_2O)$ and $G(H_2)$ are the energies of slab, H_2O and H_2.

2. Supplementary Figures

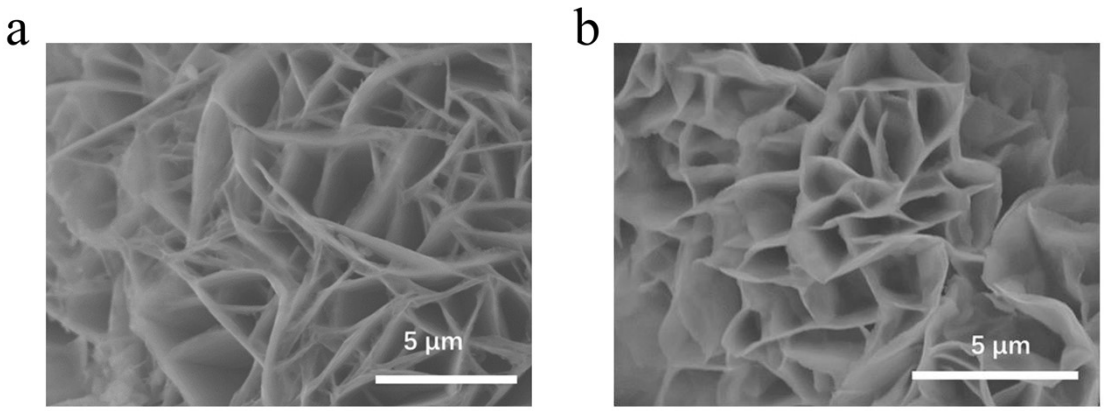

Figure S1. SEM images. (a) Zn-NiFe LDH supported on CC, (b) Zn-NiFeP/CC.

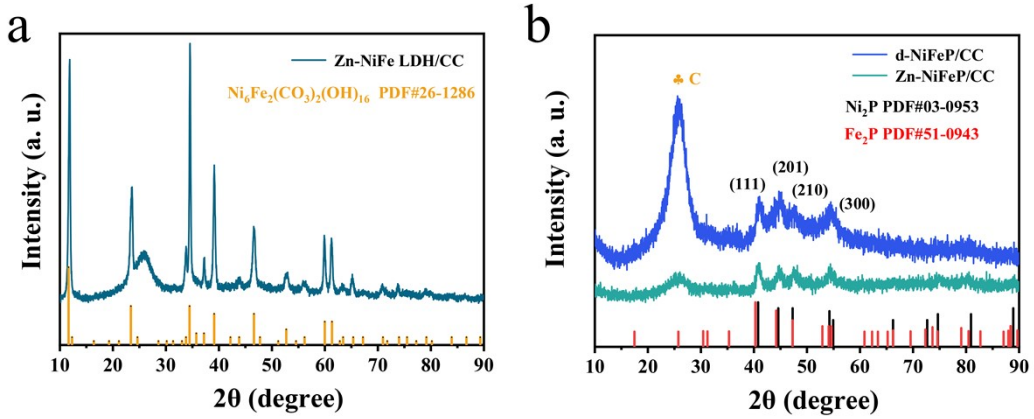

Figure S2. XRD patterns. (a) Zn-NiFe LDH/CC, (b) Zn-NiFeP/CC and d-NiFeP/CC. After phosphorization, the new diffraction peaks appear in the Zn-NiFeP pattern while the diffraction peak of Zn-NiFe LDH/CC disappears, indicating the formation of Zn-NiFeP [6-8].

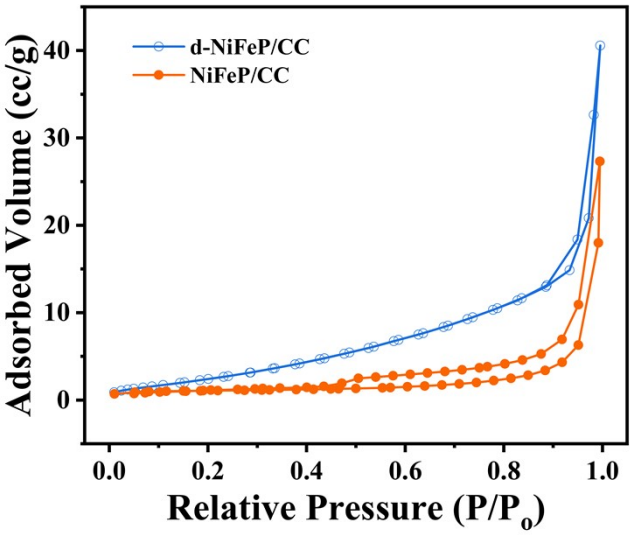

Figure S3. Nitrogen adsorption-desorption isothermal curves of d-NiFeP/CC and NiFeP/CC.

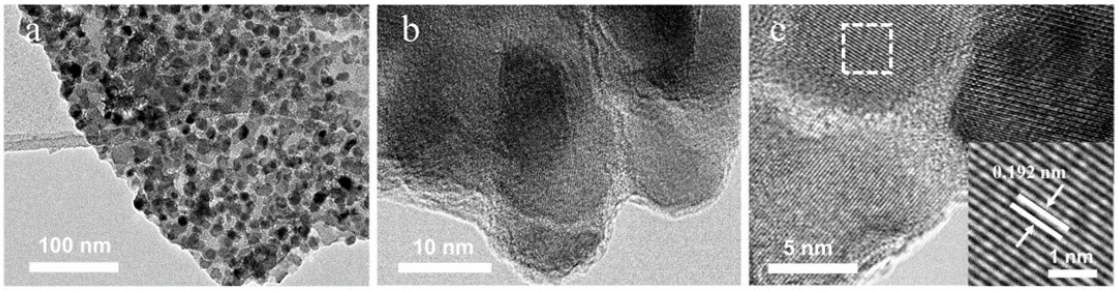

Figure S4. (a-c) Different resolutions of TEM images of NiFeP/CC.

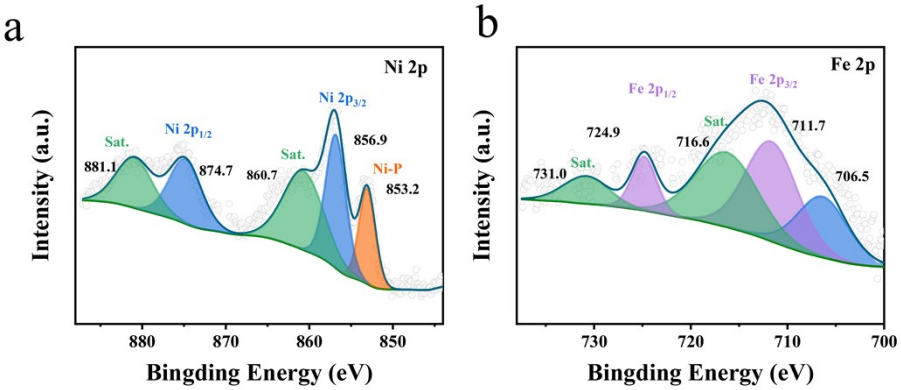

Figure S5. High-resolution XPS images of Zn-NiFeP/CC. (a) Ni 2p, (b) Fe 2p and (c) P 2p.

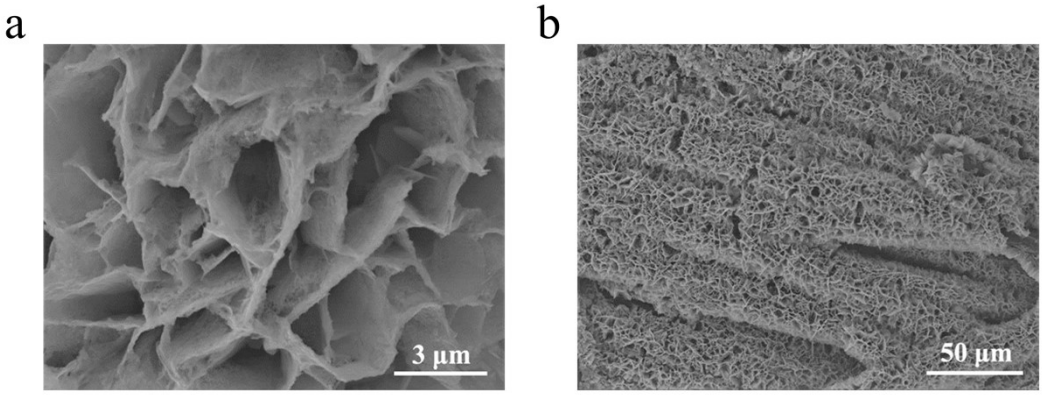

Figure S6. SEM images of d-NiFeP/CC after being maintained at 10 mA cm^{-2} for 100 h.

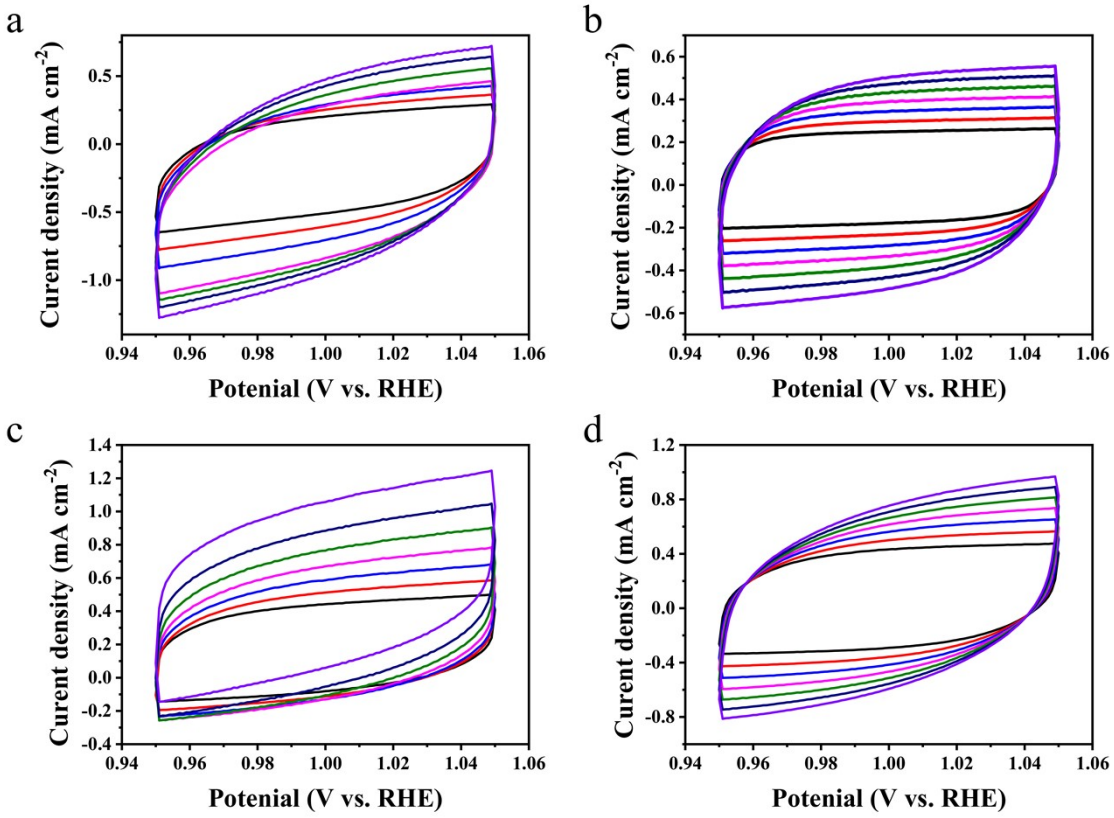

Figure S7. Cyclic voltammetry (CV) curves measured at different scan rates (40, 50, 60, 70, 80, 90, 100 mV s^{-1}). (a) d-NiFeP/CC, (b) NiFeP/CC, (c) Zn-NiFeP/CC and (d) Zn-NiFe LDH/CC.

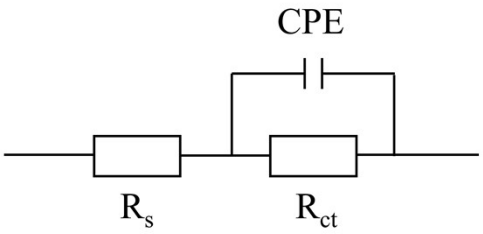

Figure S8. Nyquist diagram equivalent circuit model, where R_s is the solution resistance, R_{ct} is the charge transfer resistance and CPE is constant phase angle element.

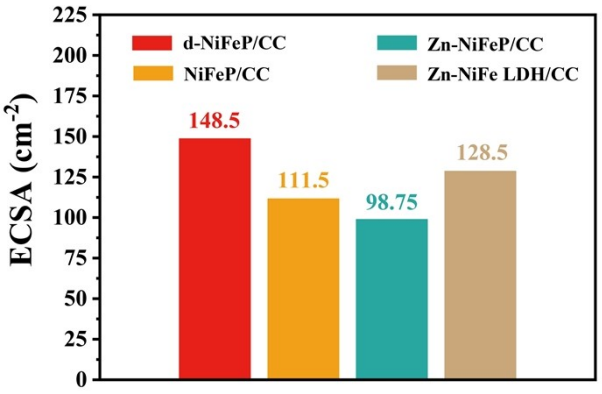

Figure S9. Electrochemically active surface area (ECSA) values of d-NiFeP/CC, NiFeP/CC, Zn-NiFeP/CC and Zn-NiFe LDH/CC.

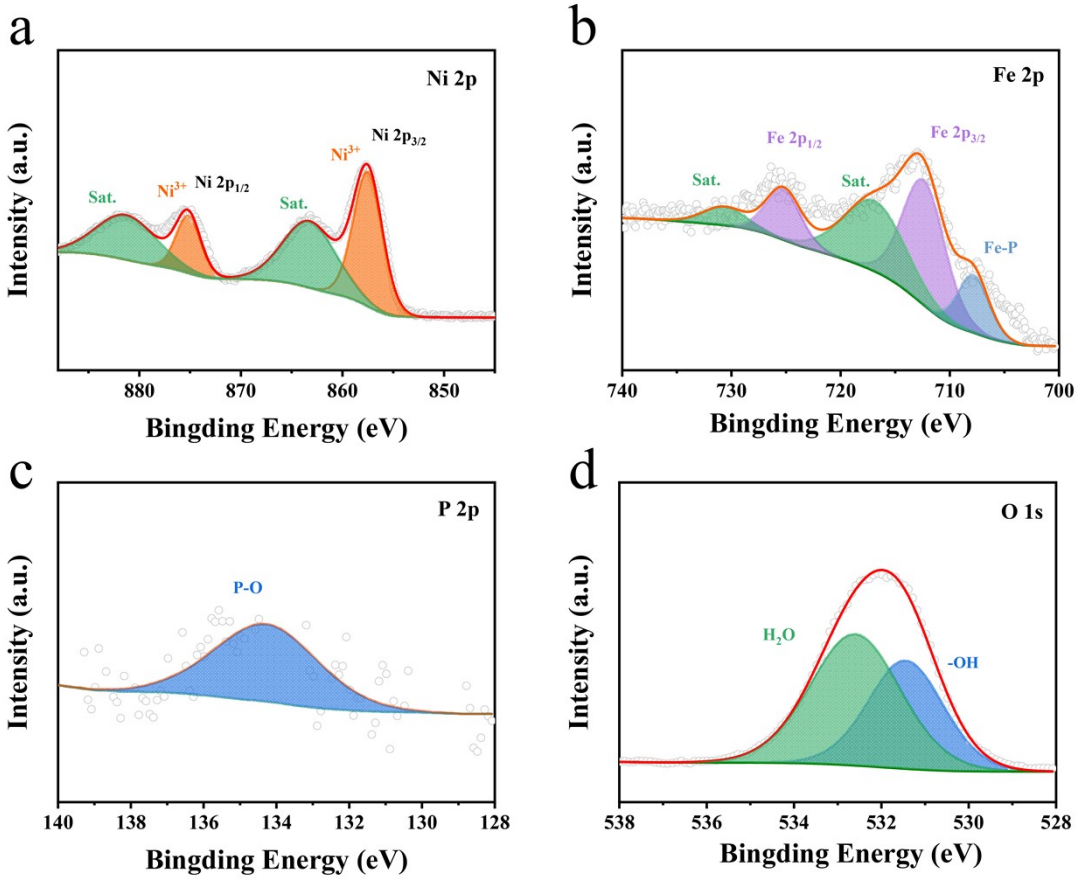

Figure S10. High-resolution XPS images of d-NiFeP/CC after stability testing (OER). (a) Ni 2p, (b) Fe 2p, (c) P 2p, and (d) O 1s.

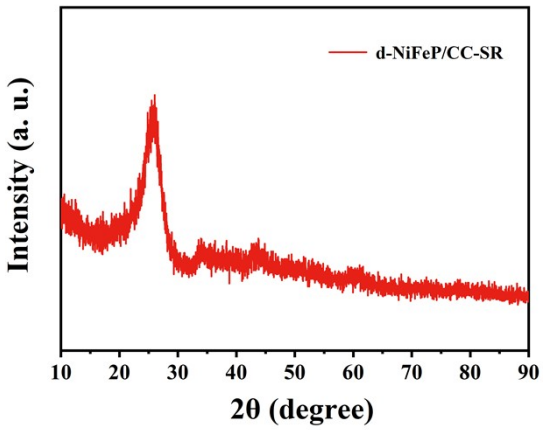

Figure S11. XRD pattern of d-NiFeP/CC after OER stability test.

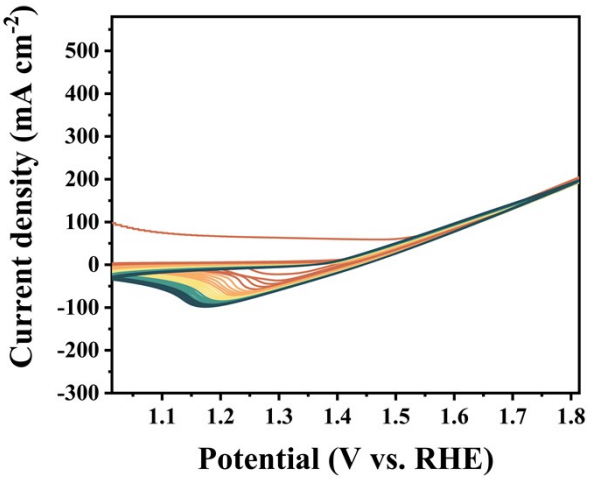

Figure S12. The first 50 CV cycles of NiFeP/CC.

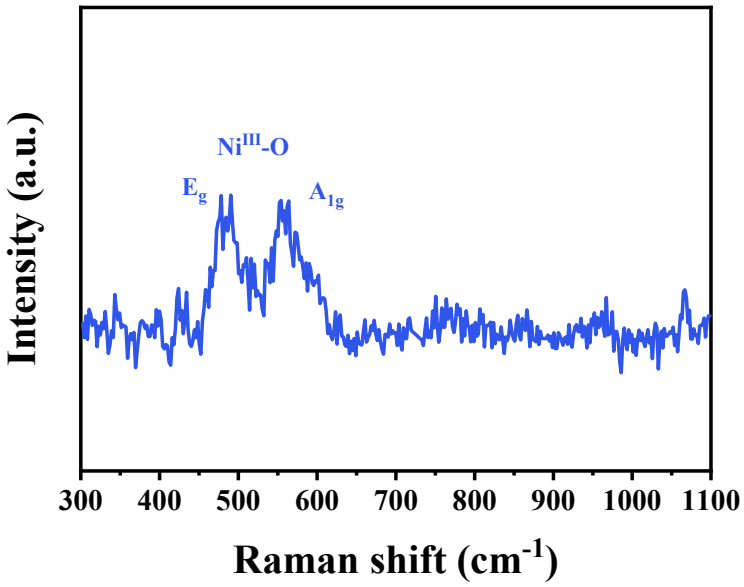

Figure S13. Raman spectra of d-NiFeP/CC after surface reconstruction (d-NiFeP/CC-SR).

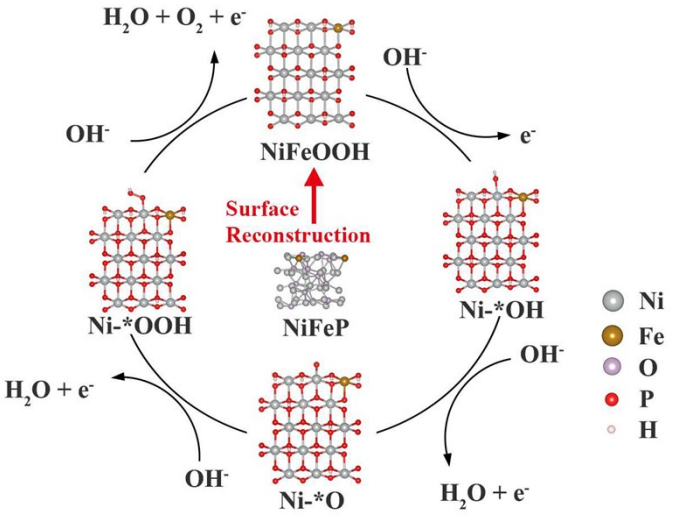

Figure S14. Schematic diagram of the reconstruction and catalytic process of surface atoms

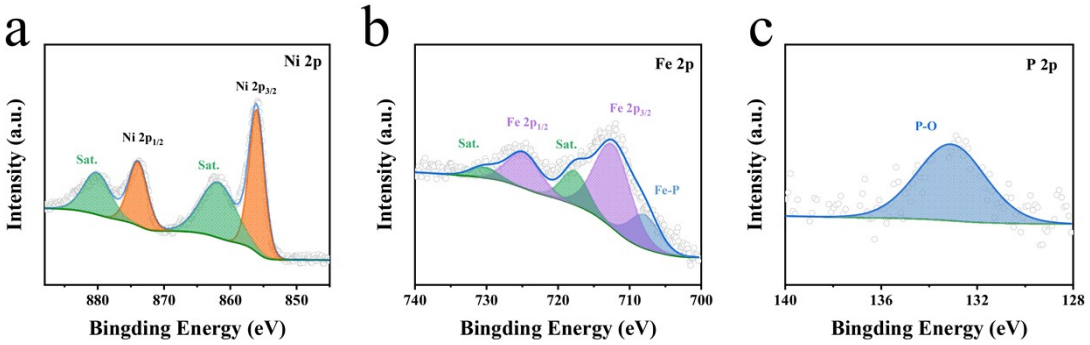

Figure S15. High-resolution XPS images of d-NiFeP/CC after stability testing (HER). (a) Ni 2p, (b) Fe 2p, (c) P 2p.

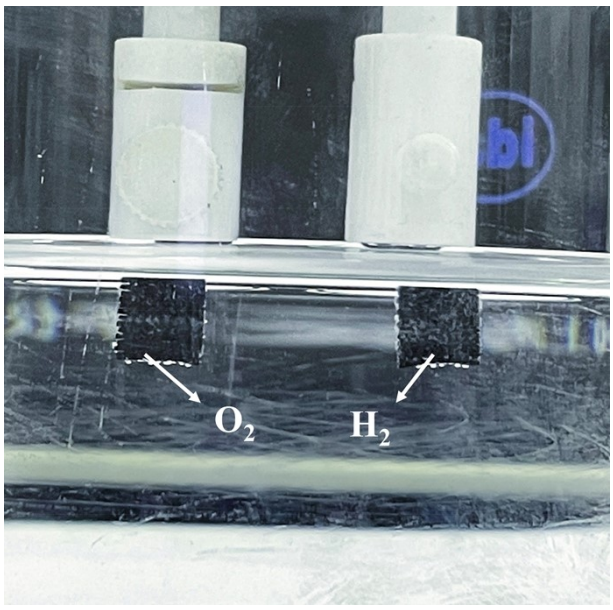

Figure S16. Image of overall-water-splitting electrolysis cell.

3. Supplementary Tables

Table S1. Weight percent of elements in Zn-NiFeP/CC measured by ICP-AES.

Element	Ni	Fe	Zn
Wt (%)	15.70	4.55	1.90

Table S2. Weight percent of elements in d-NiFeP/CC measured by ICP-AES.

Element	Ni	Fe	Zn
Wt (%)	15.18	5.12	0.06

Table S3. Elemental contents after 100 h of OER stability test measured by XPS.

Element	Ni	Fe	O	P
Atomic (%)	19.25	6.87	72.52	1.36

Table S4. Elemental contents after 50 h of HER stability test measured by XPS.

Element	Ni	Fe	O	P
Atomic (%)	17.76	6.70	72.56	2.99

Table S5. Cell voltage comparison of catalytic performance with recently reported bifunctional catalysts.

Water alkaline electrolyzer	Cell voltage (V) at 10 mA cm^{-2}	References
d-NiFeP/CC	1.486	This work
Ni_2P-Fe_2P/NF	1.561	[9]
NiP@N-CS	1.63	[10]
$(Ni_{0.75}Fe_{0.25})_2P$@GCs	1.541	[11]
Mo-doped Ni_2P HNs	1.54	[12]
MoS_2/LDH superlattice	1.57	[13]
Ni@NiFe LDH/NF	1.53	[14]
δ-FeOOH NSs/NF	1.62	[15]
NiFeRu-LDH/NF	1.52	[16]
MoP/Ni_2P/NF	1.55	[17]
$NiCo_2S_4$ NW/NF	1.63	[18]
Ni/NiP	1.61	[19]
EG/$Co_{0.85}$Se/NiFe-LDH	1.67	[20]

CC: carbon cloth., NF: nickel foam, GCs: graphitized carbon films, N-CS: N-doped carbon sponge, HNs: hollow nanostructures.

Supplementary References

1. L.-F. Li, Y.-F. Li and Z.-P. Liu, *ACS Catalysis*, 2020, **10**, 2581-2590.
2. L. Xiong, B. Wang, H. Cai, H. Hao, J. Li, T. Yang and S. Yang, *Applied Catalysis B: Environmental*, 2021, **295**, 120283.
3. T. Zhao, X. Shen, Y. Wang, R. K. Hocking, Y. Li, C. Rong, K. Dastafkan, Z. Su and C. Zhao, *Advanced Functional Materials*, 2021, **31**, 2100614.
4. Y. Hao, Y. Li, J. Wu, L. Meng, J. Wang, C. Jia, T. Liu, X. Yang, Z. P. Liu and M. Gong, *J Am Chem Soc*, 2021, **143**, 1493-1502.
5. Z. Shao, Q. Zhu, Y. Sun, Y. Zhang, Y. Jiang, S. Deng, W. Zhang, K. Huang and S. Feng, *Adv Mater*, 2022, **34**, 2110172.
6. Y. Jeung, H. Jung, D. Kim, H. Roh, C. Lim, J. W. Han and K. Yong, *Journal of Materials Chemistry A*, 2021, **9**, 12203-12213.
7. S. Sun, X. Zhou, B. Cong, W. Hong and G. Chen, *ACS Catalysis*, 2020, **10**, 9086-9097.
8. X. Wang, Q. Hu, G. Li, S. Wei, H. Yang and C. He, *Journal of Materials Chemistry A*, 2021, **9**, 15648-15653.
9. L. Wu, L. Yu, F. Zhang, B. McElhenny, D. Luo, A. Karim, S. Chen and Z. Ren, *Advanced Functional Materials*, 2020, **31**, 2006484.
10. J. Hei, G. Xu, B. Wei, L. Zhang, H. Ding and D. Liu, *Applied Surface Science*, 2021, **549**, 149297.
11. H. Zhao, Y. Wang, L. Fang, W. Fu, X. Yang, S. You, P. Luo, H. Zhang and Y. Wang, *Journal of Materials Chemistry A*, 2019, **7**, 20357-20368.
12. Q. Wang, H. Zhao, F. Li, W. She, X. Wang, L. Xu and H. Jiao, *Journal of Materials Chemistry A*, 2019, **7**, 7636-7643.
13. P. Xiong, X. Zhang, H. Wan, S. Wang, Y. Zhao, J. Zhang, D. Zhou, W. Gao, R. Ma, T. Sasaki and G. Wang, *Nano Lett*, 2019, **19**, 4518-4526.
14. Z. Cai, X. Bu, P. Wang, W. Su, R. Wei, J. C. Ho, J. Yang and X. Wang, *Journal of Materials Chemistry A*, 2019, **7**, 21722-21729.
15. B. Liu, Y. Wang, H. Q. Peng, R. Yang, Z. Jiang, X. Zhou, C. S. Lee, H. Zhao and W. Zhang, *Adv Mater*, 2018, **30**, 1803144.
16. G. Chen, T. Wang, J. Zhang, P. Liu, H. Sun, X. Zhuang, M. Chen and X. Feng, *Adv Mater*, 2018, **30**, 1706279.
17. C. Du, M. Shang, J. Mao and W. Song, *Journal of Materials Chemistry A*, 2017, **5**, 15940-15949.
18. A. Sivanantham, P. Ganesan and S. Shanmugam, *Advanced Functional Materials*, 2016, **26**, 4661-4672.
19. G. F. Chen, T. Y. Ma, Z. Q. Liu, N. Li, Y. Z. Su, K. Davey and S. Z. Qiao, *Advanced Functional Materials*, 2016, **26**, 3314-3323.
20. Y. Hou, M. R. Lohe, J. Zhang, S. Liu, X. Zhuang and X. Feng, *Energy & Environmental Science*, 2016, **9**, 478-483.